2-8

Computational Analysis of High Enthalpy Flow around Blunt Body

by

Yukimitsu Yamamoto
National Aerospace Laboratory Chofu, Tokyo, Japan

ABSTRACT

Flux-split upwind Navier-Stokes CFD code are applied to high entalpy flow around several blunt bodies. In this paper, sphere problems in DLR HEG experiments, OREX (Orbital Re-entry Experiments) flight flowfield, hyperboloid flare flows in ONER F4 experiments and 70 deg blunt body flows including base flow regions are investigated. Real gas effects are analyzed by using the one temperature chemically non-equilibrium Navier-Stokes code, which is developed by combining finite-rate chemical reactions to the current perfect gas flux splitting code. A fully implicit ADI scheme is used to avoid the stiffness problem of the time integrations. Numerical results are discussed for each flow problems and fairly good agreements are quantitatively obtained for heat transfer distributions.

Introduction

For developing and designing space transportation re-entry vehicles, accurate prediction and evaluation of hypersonic aerodynamic and aerothermodynamic characteristics are greatly important, because severe aerodynamic heating occurs and they are important research subjects for the design of thermal protection systems. For these high enthalpy re-entry flows, ground based test facilities can not simulate and reproduce realistic flight enviroments. Therefore, CFD becomes to play an important role for evaluating the aerodynamic and aerothermodynamic characteristics. However, real gas effects must be explored carefully and corresponding CFD code has to be validated by comparisons with high enthalpy wind tunnel tests and flight experiments. In our numerical code, 7 species, one temperature models are used to account for real gas effects due to dissociation and ionization, because current study is focused on the atomospheric re-entry, where thermally equilibrium state may be dominant. In addition, the difference of heat flux computed two and one temperature models may be ignored. Species mass conservation equations with source terms are combined to the present three-dimensional flux splitting Navier-Stokes equations. New algorithms for flux-splitting schemes are developed by several authors in order to decrease their dissipative features. However, in the present, these schemes may not be sufficiently established for the aerodynamic design use.

In the present study, conventional flux splitting scheme is used and the accuracy and applicability of our numerical approach are investigated . In order to avoid stiffness problems, associated with chemical reactions, fully implicit ADI method is applied.

Numerical Algorithm

Basic Equations

The three-dimensional chemically non-equilibrium Navier-Stokes equations including species continuity equations with thin-layer assumption are expressed as ;

$$\frac{\partial \overline{Q}}{\partial t}+\frac{\partial \overline{F}}{\partial \xi}+\frac{\partial \overline{H}}{\partial \eta}+\frac{\partial\left(\overline{H}-\overline{H}_{v}\right)}{\partial \zeta}=\overline{S} \qquad (1)$$

$$\overline{Q}=\begin{bmatrix}\rho_1\\ \rho_2\\ \vdots\\ \rho_n\\ \rho u\\ \rho v\\ \rho w\\ E\end{bmatrix} \qquad (2)$$

$$\overline{F}=\frac{|\nabla \xi|}{J}\begin{bmatrix}\rho_1 U\\ \rho_2 U\\ \vdots\\ \rho_n U\\ \rho u U+\tilde{\xi}_x P\\ \rho v U+\tilde{\xi}_y P\\ \rho w U+\tilde{\xi}_z P\\ (E+P)\cdot U\end{bmatrix} \qquad (3)$$

$$\overline{G}=\frac{|\nabla \eta|}{J}\begin{bmatrix}\rho_1 V\\ \rho_2 V\\ \vdots\\ \rho_n V\\ \rho u V+\tilde{\eta}_x P\\ \rho v V+\tilde{\eta}_y P\\ \rho w V+\tilde{\eta}_z P\\ (E+P)\cdot V\end{bmatrix} \qquad (4)$$

$$\overline{\boldsymbol{H}} = \frac{|\nabla\zeta|}{J}\begin{bmatrix} \rho_1 W \\ \rho_2 W \\ \vdots \\ \rho_n W \\ \rho u W + \tilde{\zeta}_x P \\ \rho v W + \tilde{\zeta}_y P \\ \rho w W + \tilde{\zeta}_z P \\ (E+P)\cdot W \end{bmatrix} \tag{5}$$

$$\overline{\boldsymbol{H}}_v = \frac{|\nabla\zeta|}{J}\begin{bmatrix} -\rho_1\left(\tilde{\zeta}_x u_{s1} + \tilde{\zeta}_y v_{s1} + \tilde{\zeta}_z w_{s1}\right) \\ -\rho_2\left(\tilde{\zeta}_x u_{s2} + \tilde{\zeta}_y v_{s2} + \tilde{\zeta}_z w_{s2}\right) \\ \vdots \\ -\rho_n\left(\tilde{\zeta}_x u_{sn} + \tilde{\zeta}_y v_{sn} + \tilde{\zeta}_z w_{sn}\right) \\ \mu\cdot|\nabla\zeta|\cdot\left(u_\zeta + W_\zeta\cdot\tilde{\zeta}_x/3\right) \\ \mu\cdot|\nabla\zeta|\cdot\left(u_\zeta + W_\zeta\cdot\tilde{\zeta}_y/3\right) \\ \mu\cdot|\nabla\zeta|\cdot\left(u_\zeta + W_\zeta\cdot\tilde{\zeta}_z/3\right) \\ |\nabla\zeta|\cdot\Theta \end{bmatrix} \tag{6}$$

$$\begin{aligned} U &= \tilde{\xi}_x u + \tilde{\xi}_y v + \tilde{\xi}_z w \\ V &= \tilde{\eta}_x u + \tilde{\eta}_y v + \tilde{\eta}_z w \\ W &= \tilde{\zeta}_x u + \tilde{\zeta}_y v + \tilde{\zeta}_z w \end{aligned} \tag{7}$$

$$\tilde{\zeta}_x = \zeta_x / \sqrt{\zeta_x^2 + \zeta_y^2 + \zeta_z^2} \;\; etc. \tag{8}$$

$$\Theta = \frac{\mu}{2}(u^2+v^2+w^2)_\zeta + k\cdot T_\zeta + \rho\sum_{i=1}^{n} h_i D_i Y_{i\zeta} + \frac{u\cdot W\cdot W_\zeta}{3} \tag{9}$$

$$\rho = \rho_1 + \rho_2 + \rho_3 + \cdots + \rho_n \tag{10}$$

$$Y_i = \rho_i / \rho \tag{11}$$

where ζ is the coodinate normal to the body surface. The vector Q consists of species density, momentum and total energy. P and ρ are the pressure and total density, respectively. μ and k are mixture viscosity and thermal conductivity. The chemical source term $\bar{s}$ has non-zero components corresponding to species conservation equations. It is written as ;

$$\overline{\boldsymbol{S}} = \frac{1}{J}\begin{bmatrix} w_1 \\ w_2 \\ \vdots \\ w_n \\ 0 \\ 0 \\ 0 \\ 0 \end{bmatrix} \tag{12}$$

where ω_i is the mass production rate of species i.

The differencing used in the present algorithm is conventional flux vector splitting. Details of this methed is described in Ref.1.

In the present analysis, the effects of multicomponent diffusion are neglected and the binary Lewis numbers for all the species are assumed to be the same, then a simple expression for the mixture's diffusion coefficients $\tilde{D}$ results

$$\tilde{D} = \frac{\tilde{\kappa}\, Le}{\tilde{\rho}\,\tilde{C}p} \tag{13}$$

where tildes denote dimensional quantities and the following nondimensionalization has been employed.

$$C_{pf} = \frac{\widetilde{C_{pf}}\,\widetilde{T^\infty}}{U^{\infty 2}} \qquad D = \frac{\tilde{D}}{\widetilde{D^\infty}} \tag{14}$$

The equations of state for mixture is written as

$$P = \frac{\beta_1\,\rho\, T}{M} \qquad M = \frac{\widetilde{M}}{\widetilde{M^\infty}} \tag{15}$$

where the mixture molecular weight is determined by

$$M = \left(\sum_{i=1}^{n}\frac{Y_i}{M_i}\right)^{-1} \tag{16}$$

Here,Y_i is the species mass fraction and defined as ρ_i/ρ. The expression for total enthalpy is

$$H = \frac{E+P}{\rho} = h + \frac{1}{2}\left(u^2+v^2+w^2\right) \tag{17}$$

The enthalppy of the mixture is determined by summing the individual contributions of each species.

$$\tilde{h} = \sum_{i=1}^{h} Y_i\,\tilde{h}_i \tag{18}$$

$$\tilde{h}_i = \widetilde{h_{i0}} + \int_0^{\tilde{T}} \widetilde{C_{pi}}\, d\tilde{T} \tag{19}$$

The dimensional enthalpies and specific heat of each species are determined by using equations of Ref.23.

Transport Properties

The viscosity of a species, s, is calaculated using the following curve fit.

$$\tilde{\mu}_s = 0.1 exp\left[\left(A_s log_e\tilde{T} + B_s\right) log_e\tilde{T} + C_s\right] \tag{20}$$

where A_s, B_s,and C_s are constants for each species.

Eucken's formula is used to compute thermal conductivity.

$$\tilde{\kappa}_s = \frac{\tilde{\mu}_s \tilde{R}}{\widetilde{M}_s}\left(\tilde{C}_{p,s}\frac{\widetilde{M}_s}{\tilde{R}} + \frac{5}{4}\right) \tag{21}$$

Wilke's mixing rule is used to compute the mixture viscosity and thermal conductivity from those of the individual species.

$$\tilde{\mu} = \sum_{s=1}^{n} \frac{X_s \tilde{\mu}_s}{\phi_s} \qquad \tilde{\kappa} = \sum_{s=1}^{n} \frac{X_s \tilde{\kappa}_s}{\phi_s} \tag{22}$$

where

$$\begin{aligned} \phi_s &= \sum_{\gamma=1}^{n} X_\gamma \left[1 + \sqrt{\frac{\tilde{\mu}_s}{\tilde{\mu}_\gamma}}\left(\frac{M_s}{M_\gamma}\right)^{\frac{1}{4}}\right]^2 \left[\sqrt{8}\sqrt{1+\frac{\widetilde{M}_s}{\widetilde{M}_\gamma}}\right]^{-1} \\ X_s &= \frac{Y_s \widetilde{M}}{\widetilde{M}_s} \end{aligned} \tag{23}$$

Chemical Model

The chemistry model is air and 7 chemical species are taken into account ;

(1) molecular oxygen	O_2
(2) atomic oxygen	O
(3) molecular nitrogen	N_2
(4) atomic nitrogen	N
(5) nitric oxide	NO
(6) nitric oxide ion	NO^+
(7) ion	e^-

An assumption employed in this model is that the gas possesses a zero net local charge. This allows the conservation of electron mass equation to be eliminated from the set of governing equations. The reactions that are considered are ;

$$\begin{aligned} O_2 + M &= O + O + M \quad (R1) \\ N_2 + M &= N + N + M \quad (R2) \\ NO + M &= N + O + M \quad (R3) \\ NO + O &= N + O_2 \quad (R4) \\ O + N_2 &= N + NO \quad (R5) \\ O + N &= NO^+ + e^- \quad (R6) \end{aligned}$$

where impacting body M can be any one of the species. The forward and backward reaction ratets are of the form.

$$kf(T) = CfT^{nf}e^{-\theta d/T} \qquad kb(T) = \frac{kf(T)}{K_{eq}(T)} \tag{24}$$

where K_{eq} is the equilibrium constants and a function of temperature.

$$\begin{aligned} K_{eq}(T) &= exp(A1 + A2z + A3z^2 + A4z^3 + A5z^4) \\ z &= \frac{10000}{T} \end{aligned} \tag{25}$$

All the constants appearing in the reaction rate equation are given by Park.

Then, the production of species from each reaction can be expressed as ;

$$\begin{aligned} R1 &= \sum_M [-kf_{1M}[N_2][M] + kb_{1M}[N][N][M]] \\ R2 &= \sum_M [-kf_{2M}[O_2][M] + kb_{2M}[O][O][M]] \\ R3 &= \sum_M [-kf_{3M}[NO][M] + kb_{3M}[N][O][M]] \\ R4 &= -kf_4[NO][O] + kb_4[N][O_2] \\ R5 &= -kf_5[O][N_2] + kb_5[N][NO] \\ R6 &= -kf_6[N][O] + kb_6[NO^+][e^-] \end{aligned} \tag{26}$$

The souce tetrms are given by

$$\begin{aligned} w_N &= M_N(-2R1 - R3 - R4 - R5 - R6) \\ w_{N_2} &= M_{N_2}(R1 + R5) \\ w_O &= M_O(-2R2 - R3 + R4 + R5 + R6) \\ w_{O_2} &= M_{O_2}(R2 - R4) \\ w_{NO} &= M_{NO}(R3 + R4 - R5) \\ w_{NO+} &= M_{NO+}(-R6) \\ w_{e-} &= M_{e-}(-R6) \end{aligned} \tag{27}$$

Numerical Results

Numerical calculations were performed for high enthalpy flow around four type of blunt bodies. In the present study, non-equilibrium flow analysis were made for sphere (Problem I-1~6), OREX (Problem II-1,2) and hyperboloid flare (Problem III-2). Non-react perfect gas flow analysis were also made for OREX (Problem II-5) and 70 deg blunt cone. Final computational test case is not listed in the workshop problems. However, preliminaly investigation was made to find the real gas effects through comparisons of experiental data.

Sphere

Figure 1 shows pressure contours around sphere for Problem I-1 (high enthalpy, low density case),Problem I-3 (high enthalpy, high density case). Similar results can be observed for these pressure contours. However, mass fraction distributions along the stagnation stream line indicate different characteristics in each flow cases. As for the N_2 (Nitrogen molecule) mass fraction distributions of Fig.2, strong dissociation occurs in high enthalpy, high density case (Problem I-3). In the low enthalpy case (Problem I-5), significant dessociation of N_2 dose not occur compared to the other high enthalpy cases (Problem I-1 and I-3). Heat transfer distributions along the sphere surface are shown in Fig.3. In the figure, non-catalytic and full catalytic heat transfer in are plotted for the same free stream condition case. Solid line represents the sphere geometry. Dot-dash line indicates the full catalytic heat transfer distributions and dotted line shows non catalytic ones. It is remarked that full catalytic heat transfer is about two times larger than the non-catalytic one for all three flow conditions. In addition, maximum peak of heat transfer distributions appears away from the stagnation point. These flow phenomena may be caused by very low Reynolds number effects. Experimental results shows the similar tendency, however, further investigation must be done. Quantitative comparisons of full catalytic heat transfer distributions are made and presented in Fig.4. Open symbols shows experimental data and closed ones are numerical results. Relatively good agreements are obtained, especially in high enthalpy, high density flow case. However, the difference between numerical and experimental results exists in low enthalpy flow case. Detailed investigation of may be needed in this case.

OREX

In OREX flow fields calculations, 41 grid points are distributed surface and 60 points normal to be body. Temperature contours are plotted in Fig.5. From this figure, it is noticed that shock wave is smeared in high altitude case (Problem II-1) and shock also it is clearly observed that layer thickness of the reacting flow case (problem II-2) is smaller than that of corresponding perfect gas case (Problem II-5). Heat transfer distributions are plotted in Fig.6. The value of maximum stagnation point heat transfer is increased as the altitude becomes lower and 0.344 MW/m^2 at an altitude of 60 km. These values may be considered reasonable compared to the other numerical results and flight data estimations. Temperature and mass fraction distributions along the stagnation stream line are plotted in Fig.7 and 8 for the reacting flow cases of Problem II-1 and II-2.

It is remarked that shock wave region is smeared at high altitude due to the rarefaction effects. Maximum temperature in high altitude case is about two times larger than that of the low alttitude one and it reaches to more than 20,000 K. Dissociation of nitrogen molecule N_2 in high altitude is enhanced by the these high temperature effects.

Hyperboloid Flare

For this analysis, 262 (streamwise) × 51 (normal to the body) grid points are used. Pressure and temperature contours are shown in Fig.9 and Fig.10. Recompression shock wave is generated above the flare part. Pressure and heat transfer distributions are plotted in Fig.11 and Fig.12. High pressure comparable to the nose stagnation point value is caused on the flare part and small recirculation region appears ahead of the juncture point of foreward body and flare. Heat transfer is also increased, corresponding to this pressure rise. However, the peak value is about 40 percent of stagnation point one. Detailed comparison are underway and will be presented in near future. This time rough calculation is made for the preliminaly estimation. More precise and large scale computation will be done.

Blunt Cone

In this case, omly perfect gas calculations were conducted. Computational grid consists of 161 (streamwise) × 121 (normal to the body) points. In Fig.13 and Fig.14, pressure and temperature contours are depictetd, where recompression shock wave is generated from the mid region of the afterword cylinder surface. As shown in Fig.15, surface pressure and heat transfer becomes high there. The value of local peak is about 0.2, nondimensionalized by the stagnation point heating. These results are similar to the LaRC low enthalpy hypersonic wind tunnel experiments [2]. More detailed comparisons will be made in near future.

Conclusions

By using the flux-split upwind Navier-Stokes code, several blunt body problems, proposed in NAL high enthalpy flow workshop, are analyzed. Our approach is one temperature, chemically non-equilibrium computational method for reacting flow problems. This is not sufficient for the exact analysis of high enthalpy flow phenomena. However, in practical purposes, it is useful in evaluating aerothermodynamic characteristics, because the siginificant difference of heat transfer is not observed between one-temperature and two-temperature models. Therefore, we try first the simple one temperature modeling for high enthalpy flow analysis and the limitations of this modeling is investigated.

In the present preliminary studies, numerical results favorably predict heat transfer distributions of four type of blunt bodies. However, these problems contain difficult phenomena to analyze, such as surface catalycity, the effects of the flow separation and reattachment, base flow problems etc. So, more precise study and exact validation of the CFD code will be needed.

References

1) Y.Yamamoto, "Numerical Simulation of Hypersonic Viscous Flow for Design of H-II Orbiting Plane (HOPE), Part II." AIAA Paper 91-1390, June, 1991

2) D.Kastel, T.J.Harvath, and G.Eitelberg "Non-equilibrium Flow Expansion Experiment around a Blunted Cone." Proc. of Second European Symp. on Aerothermodynamics for Space Vehicles. ESTEC, Noordwijk, The Netherlands, 21-25 Nov. 1994, ESASP-367, pp 383-389

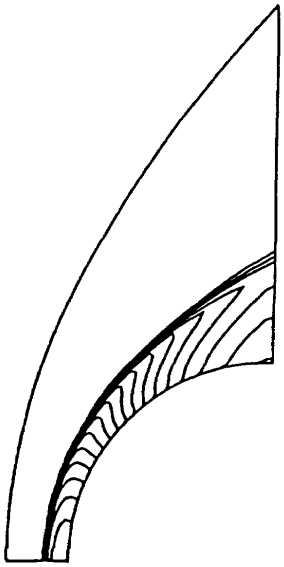

(a) Problem I-1 Sphere Pmax=0.944
Pressure Contour Non catalytic
V_∞=5939m/s T_∞=705K
ρ_∞=0.00158 T_{wall}=300K

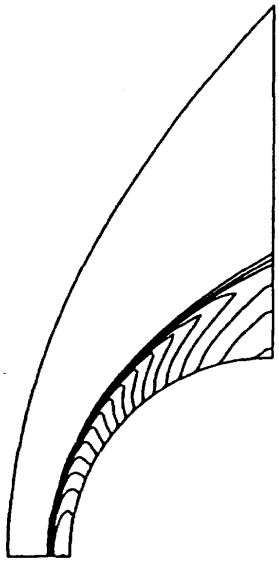

(b) Problem I-3 Sphere Pmax=0.957
Pressure Contour Non catalytic
V_∞=6180m/s T_∞=934K
ρ_∞=0.0034 T_{wall}=300K

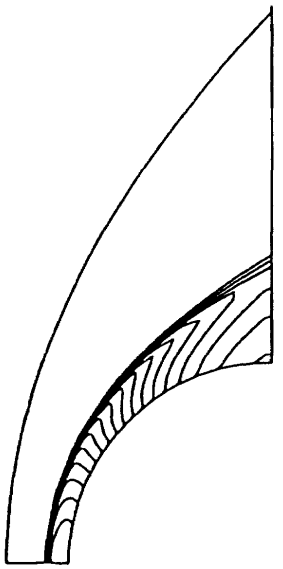

(c) Problem I-5 Sphere Pmax=0.950
Pressure Contour Non catalytic
V_∞=5151m/s T_∞=708K
ρ_∞=0.0058 T_{wall}=300K

Fig.1 Pressure Contour around Sphere

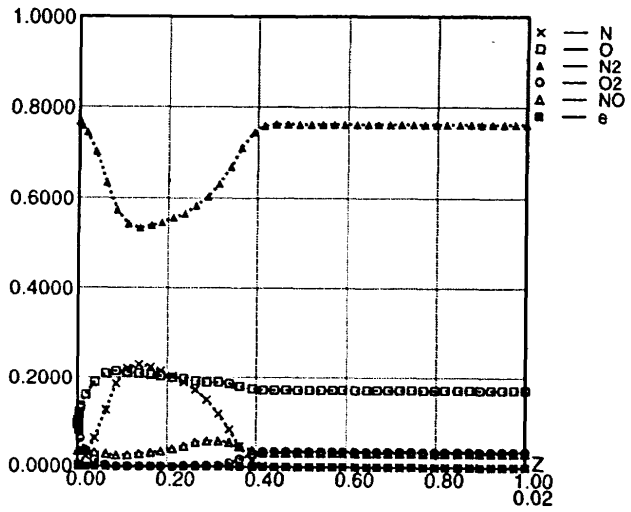

(a) Problem I - 1 Sphere Non Catalytic

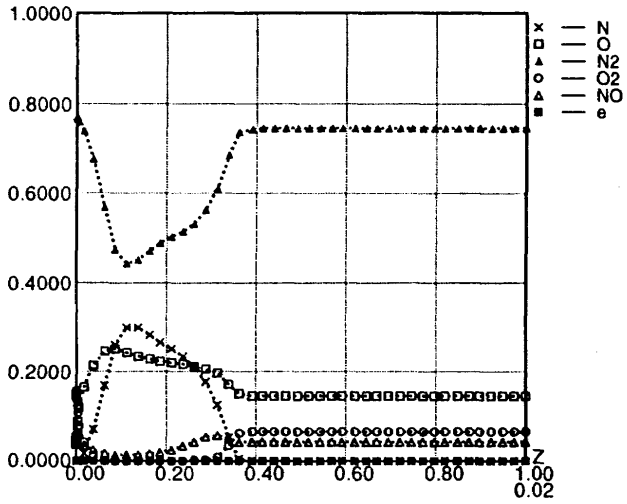

(b) Problem I - 3 Sphere Non Catalytic

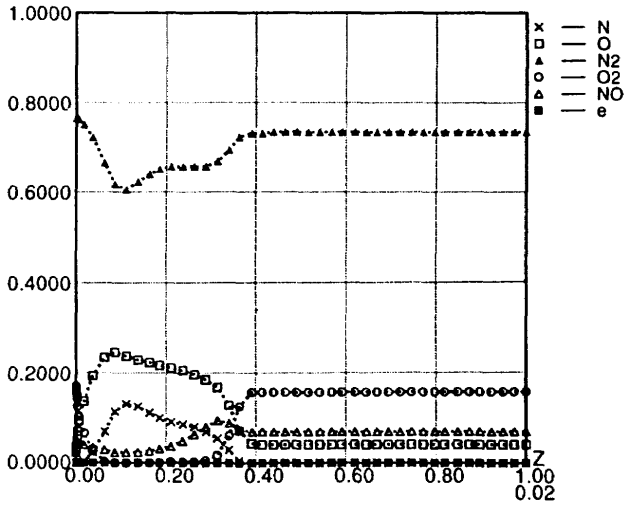

(c) Problem I - 5 Sphere Non Catalytic

Mass Fraction along the Stagnation Stream Line

Fig.2

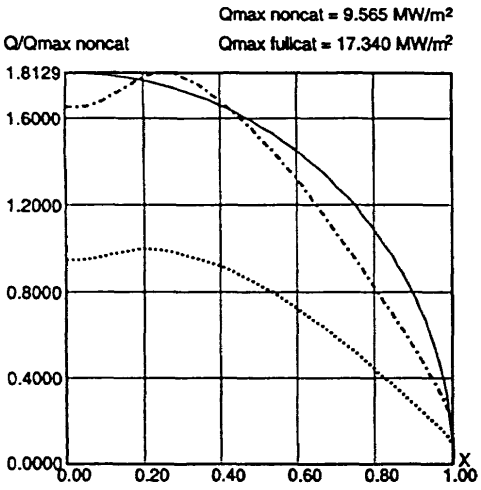

(a) Problem I - 1,2 Sphere Heat Transfer Distribution

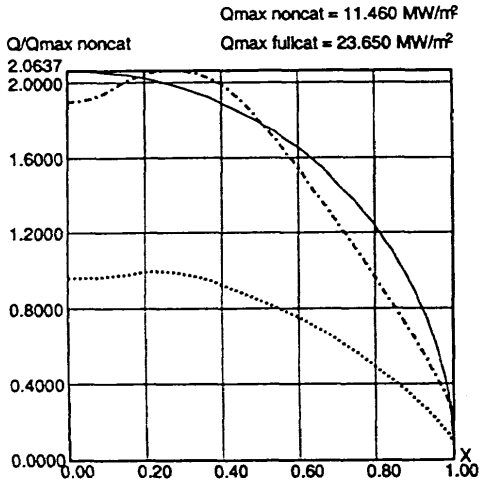

(b) Problem I - 3,4 Sphere Heat Transfer Distribution

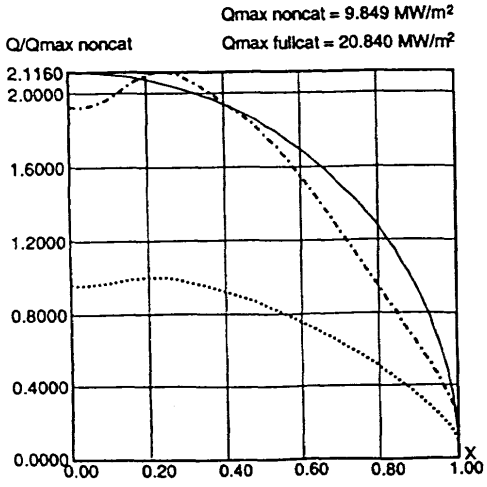

(c) Problem I - 4,5 Sphere Heat Transfer Distribution

Fig.3

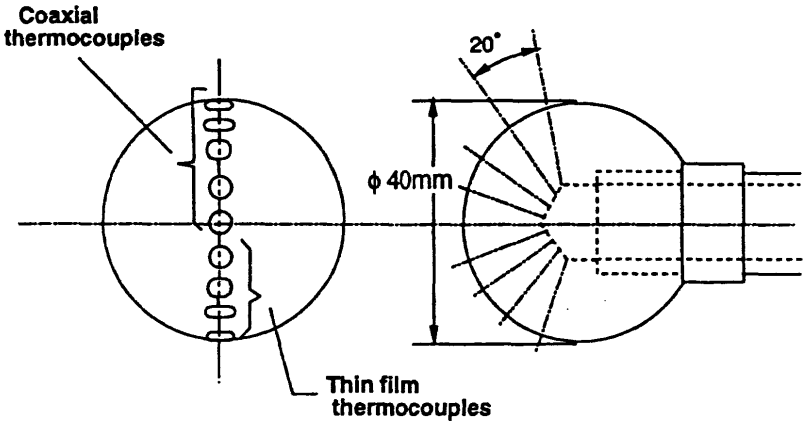

Sphere model

1.1.2 Test Cases

Case	V ∞	T ∞	ρ ∞ (kg /m ³)	Twall	Modelization	Level
I-1	5939m/s	705K	0.00156	300K	Lam, Non-eq, Non-cat	•••
I-2	//	//	//	//	// Full-cat	•••
I-3	6180m/s	934K	0.0034	300K	Lam, Non-eq, Non-cat	•••
I-4	//	//	//	//	// Full-cat	•••
I-5	5151m/s	708K	0.0058	300K	Lam, Non-eq, Non-cat	•••
I-6	//	//	//	//	// Full-cat	•••

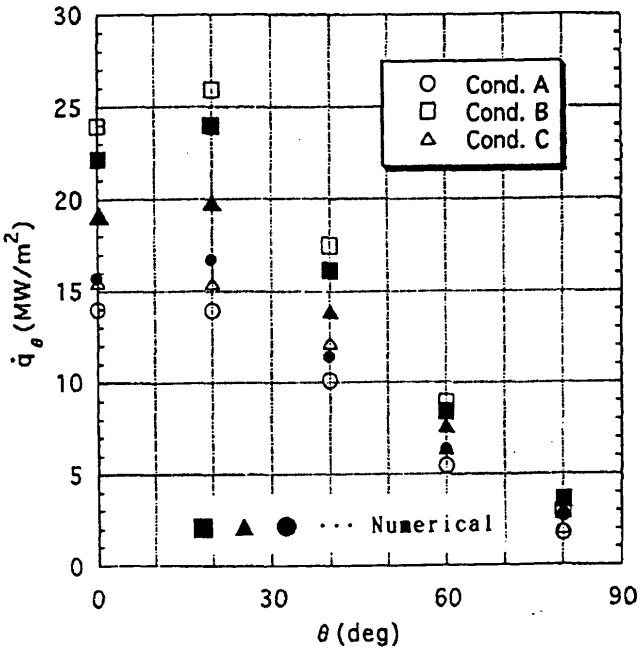

Fig.4 Comparison of Heat Transfer with HEG Experiments

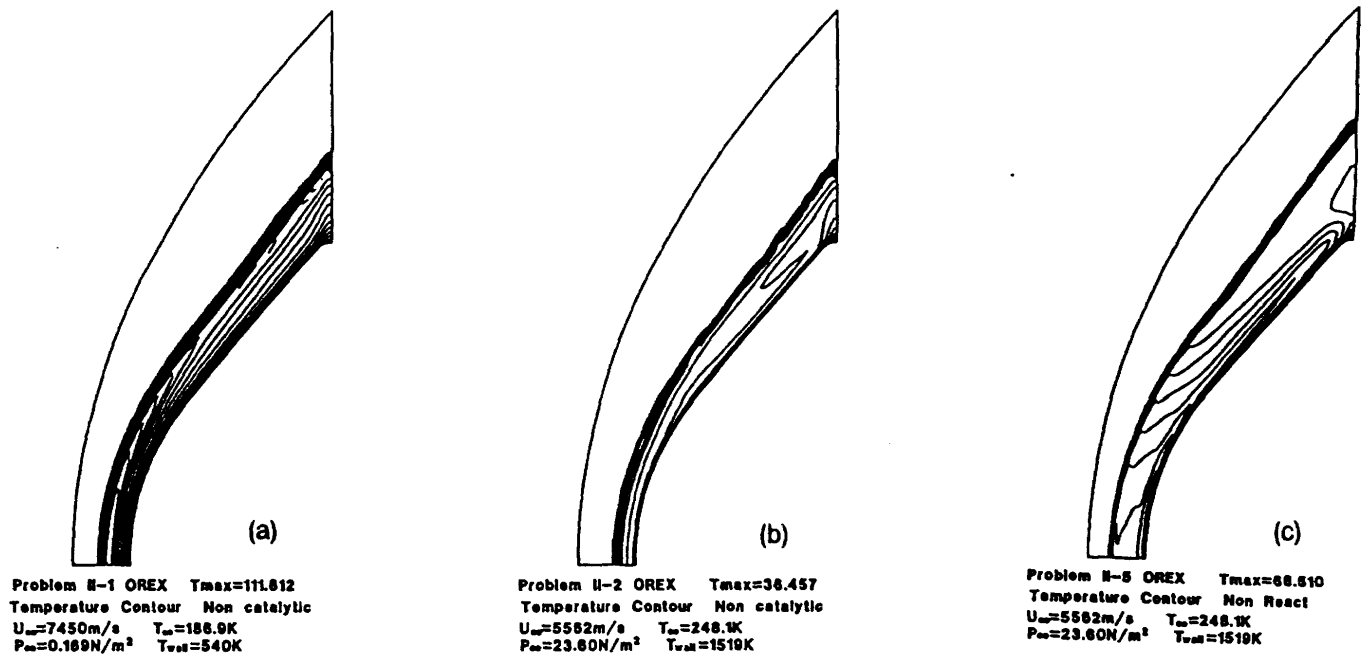

Fig.5 Temperature Contour around OREX

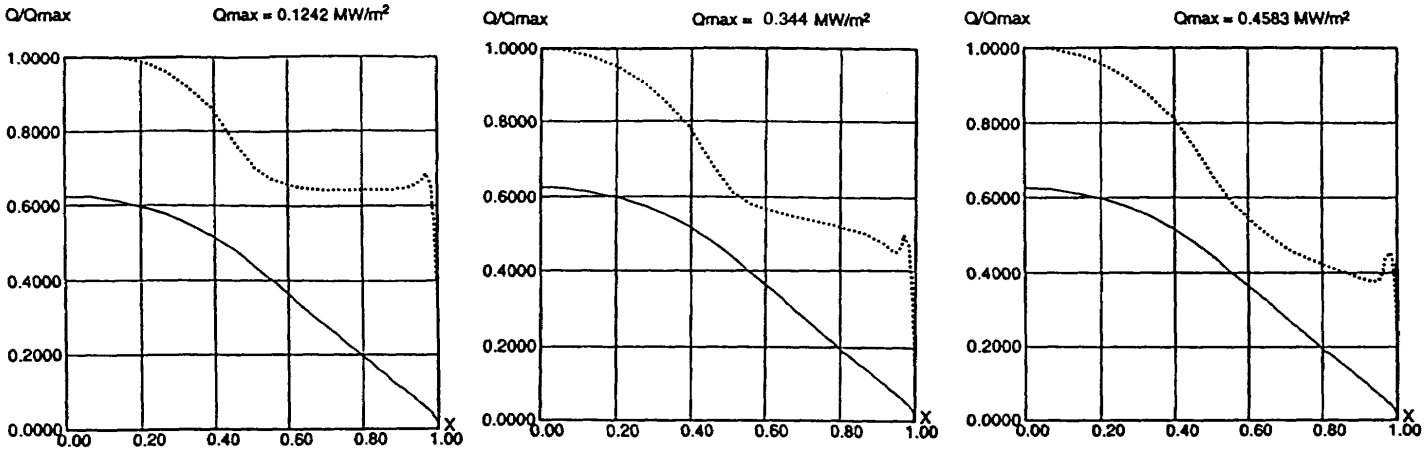

(a) Problem II - 1 OREX (b) Problem II - 2 OREX (c) Problem II - 5 OREX

Fig.6 Heat Transfer Distribution

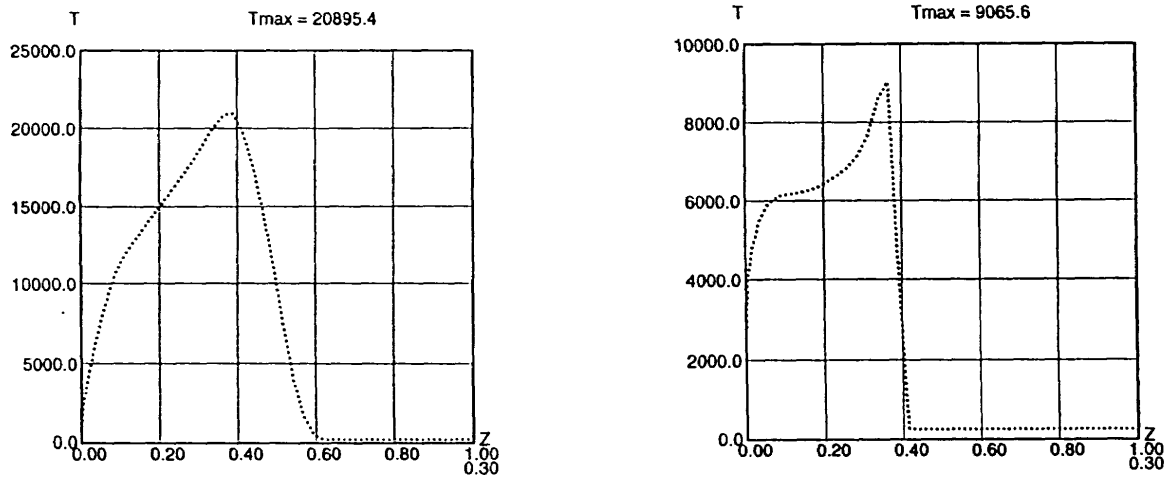

Problem II - 1 -⑥ OREX
Non Catalytic Case
Stagnation Line Temperature Distribution

Problem II - 2 -⑥ OREX
Non Catalytic Case
Stagnation Line Temperature Distribution

Fig.7

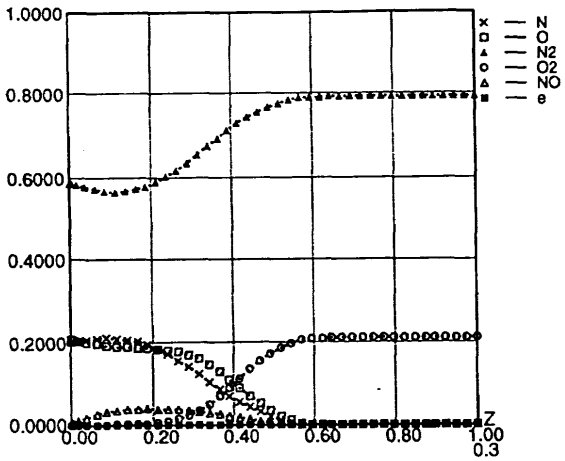

Problem II - 1 OREX Non Catalytic

Mass Fraction along the Stagnation Stream Line

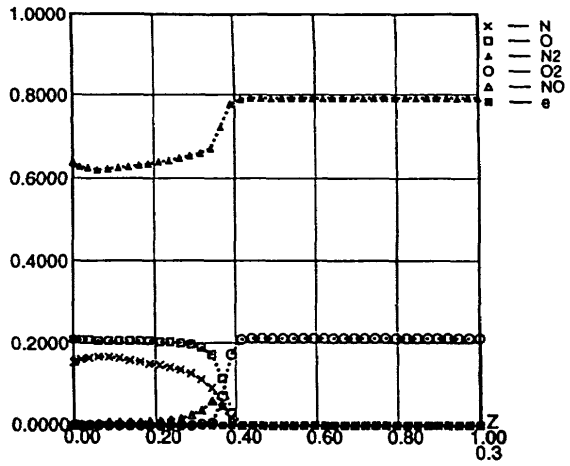

Problem II - 2 OREX Non Catalytic

Mass Fraction along the Stagnation Streem Line

Fig.8

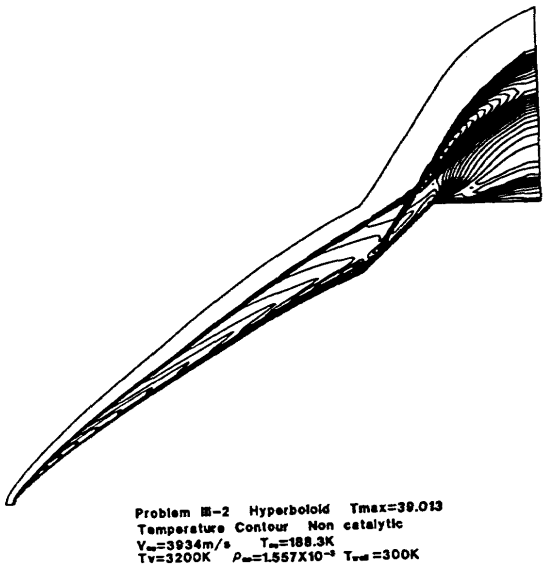

Fig.9

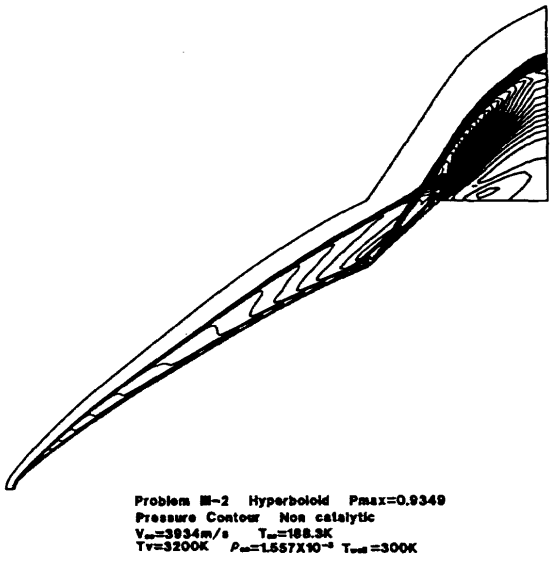

Fig.10

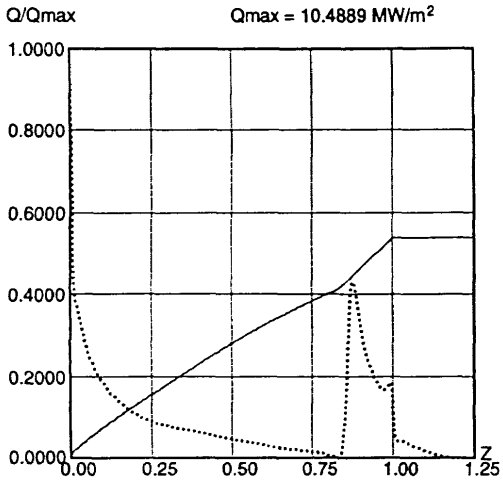

Problem III - 2 Hyperboloid Flare

Heat Transfer Distribution

Fig.11

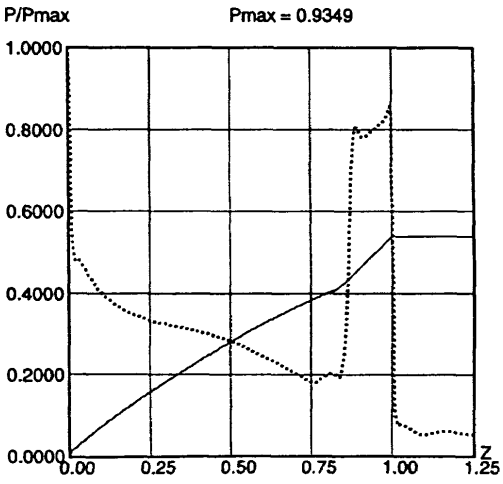

Problem III - 2 Hyperboloid Flare

Pressure Distribution

Fig.12

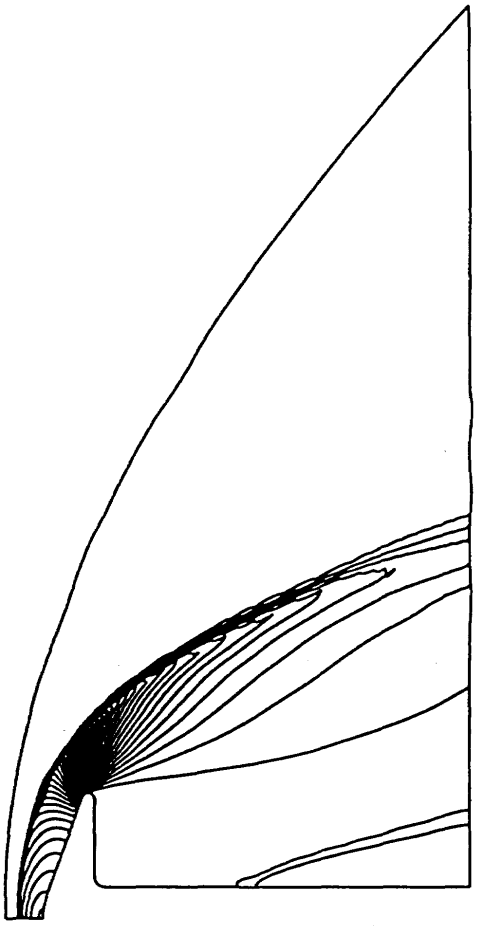

Fig.13

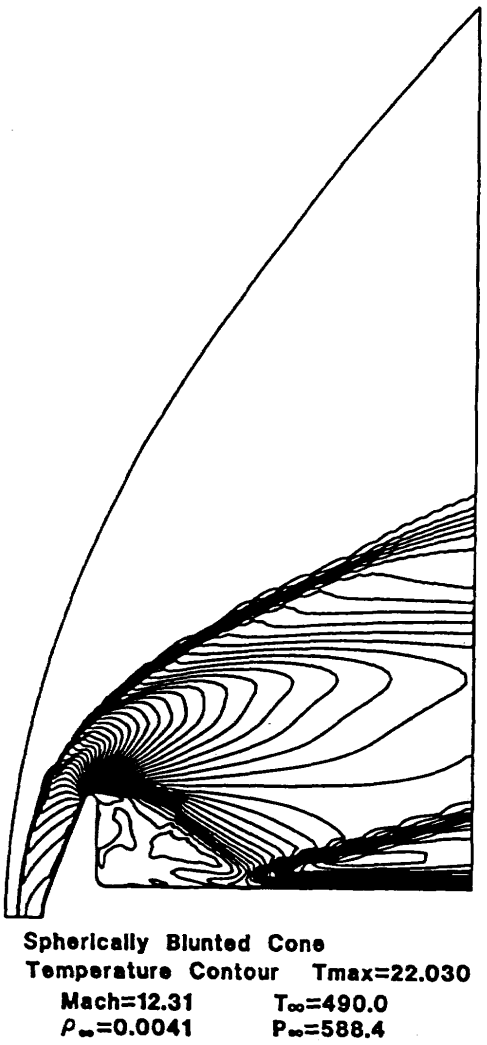

Fig.14

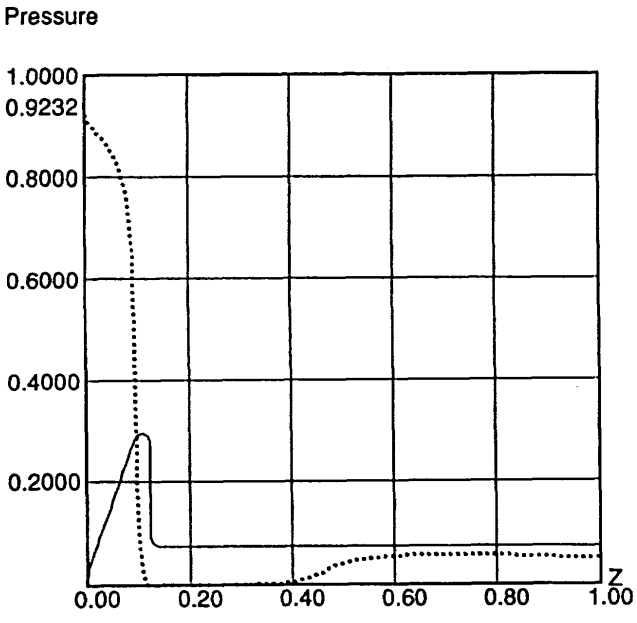

(a) Pressure Distribution

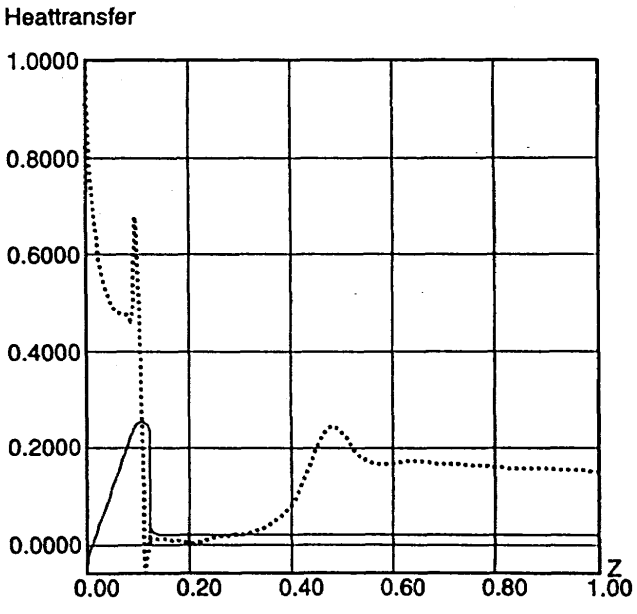

(b) Heat Transfer Distribution

Fig.15